HHS Public Access

Author manuscript

Int Symp Med Robot. Author manuscript; available in PMC 2023 December 08.

Published in final edited form as:

Int Symp Med Robot. 2023 April ; 2023: . doi:10.1109/ismr57123.2023.10130240.

Open Source MR-Safe Pneumatic Radial Inflow Motor and Encoder (PRIME): Design and Manufacturing Guidelines

Anthony L. Gunderman,
Georgia Tech Institute for Robotics and Intelligent Machines (IRIM), Atlanta, GA 30313, USA

Milad Azizkhani,
Georgia Tech Institute for Robotics and Intelligent Machines (IRIM), Atlanta, GA 30313, USA

Saikat Sengupta,
Vanderbilt University Institute of Imaging Science, Vanderbilt University Medical Center, Nashville, TN 37232 USA

Kevin Cleary,
Children's National Hospital, Washington, DC 20010 USA

Yue Chen
Georgia Tech Institute for Robotics and Intelligent Machines (IRIM), Atlanta, GA 30313, USA

Abstract

Actuators and encoders used in MR-guided robotic interventions are subject to strict requirements to ensure patient safety and MR imaging quality. In this paper, we present an open source computer aided design (CAD) of our MR-safe Pneumatic Radial Inflow Motor and Encoder (PRIME). PRIME is a parametrically designed motor that enables scalability based on torque and speed requirements for a wide range of MR-guided robotic procedures. The design consists of five primary modifiable parameters that define the entire motor geometry. All components of the motor are either 3D printed or available off-the-shelf. Quadrature encoding is achieved using a 3D printed housing and four fiber optic cables. Benchtop experiments were performed to validate the performance of the proposed design. To the best of our knowledge, this is the first open source MR-safe pneumatic motor and encoder in the field. We aim to share the design and manufacturing guidelines to lower the entry barriers for researchers interested in MR-guided robotics.

I. Introduction

Magnetic Resonance (MR) -guided robotic interventions have attracted significant research attention in the last several decades [1]. By integrating the advantages of high-resolution imaging feedback with compact and precise robots, state-ofthe-art robotic systems have been proposed in several MR-guided clinical procedures. These include epilepsy ablation [2], intracerebral hemorrhage removal [3], [4], [5], tumor ablation [6], prostate biopsy [7], gynecological brachytherapy [8], [9], [10], lower back pain injections [11], generalized needle interventions [12], and more [13]. Despite increasing prevalence, generalized

Corresponding Author: Yue Chen yue.chen@bme.gatech.edu.

adoption of MR-guided robotic interventions is limited by the stringent requirements of the MR environment and review/standards criteria from the FDA [14] and ASTM [15], [16], [17]. Specifically, standard DC motors and encoders are not applicable for use inside the MRI without appropriate protections and shielding techniques.

This has motivated many research groups to investigate safe and effective MR-safe/conditional actuation approaches [19]. One such alternative is the use of piezoelectric motors, which rely on the piezoelectric effect to induce strain in crystal materials to generate motion. Several groups have used piezoelectric motors for MR-guided interventions, including transrectal prostate needle placement [20], deep brain stimulation [21], lumbar needle placement [11], and shoulder arthrography procedures [22]. However, piezoelectric motors rely on a variable electric waveform, which can result in a reduction in signal-to-noise ratio (SNR) and often precludes real-time imaging in MRI [23]. Additionally, piezoelectric motors and their electronic drivers are often costly (> $1500) and require significant production lead time (8-weeks).

To circumvent the limitations associated with piezoelectric motors, pneumatic-driven actuators have been developed for MR-guided robots. These include (i) deformation-based stepper actuation, (ii) non-deformation based stepper actuation, and (iii) continuous-based actuation [19]. Deformationbased stepper actuation uses case-specific geometry, such as bellows [24], [25] or auxetic structures [26], to generate stepwise motion. However, these devices are typically designed for a specific task and are difficult to be scaled/modified for generalized clinical adoption. Non-deformation based stepper actuation relies on either custom gear teeth [27], [28], [29] or pistons [30], [31] to obtain step-wise motion. These motors typically require short pneumatic hose length (< 3-m) during implementation, requiring proper shielding of the pneumatic valves inside the scanner room. Continuous based actuation implements either double acting cylinders [32], [33], [34] or novel turbine based designs [18], [35]. Double acting pneumatic cylinders are often cumbersome and limited to linear motion [32]. Of the alternatives listed above, turbine based motor designs present significant promise in enabling generalized adoption of MR-guided robotic interventions, allowing continuous output torque and real-time imaging during interventions [5].

In this paper, we provide an open source design and fabrication guidelines of an MR-safe Pneumatic Radial Inflow Motor and Encoder (PRIME) that can be generalized and scalable for a variety of MR-guided robotic interventions (see Fig. 1). The motor parametric design uses five primary design parameters that define the entire motor geometry using global variables in SolidWorks™. The contributions of this work include the following: (1) open source of the motor CAD for use in MR-guided interventions, (2) open source fabrication instructions of the motor and optical encoder, and (3) parameter selection guidance based on required torque and speed needs. The manuscript is arranged as follows. Section II discusses the pneumatic motor and encoder design, and general guidance for design parameter selection. Section III discusses fabrication instructions and guidelines for motor and encoder assembly. Section IV presents torque and power curves of the motors in Fig. 1, MRI characterization, and a discussion of possible use cases. The paper is concluded in Section V.

II. Hardware Design

A. Motor Design

The motor design used herein is developed based on our prior work [18]. However, we have incorporated design modifications to improve scalability and operation efficiency. These include (i) parametric modeling using five primary modifiable parameters (rotor outer diameter, inner diameter, and length, nozzle angle of attack, and nozzle diameter) in SolidWorks™ to enable scalability of the motor, and (ii) the inclusion of exhaust ports that leave axially from the periphery of the gearbox cross-section m.

The motor is considered a radial inflow turbine [36] that consists of a stator, cap, and rotor, all 3D-printed using either Tough 2000 or Clear resin with a FormLabs 3D printer (Form 3B, FormLabs, MA, USA) (Fig. 2A). The smallest feasible motor size is 28 mm in diameter and 30 mm long (not including pneumatic attachment and gearbox flanges). This dimension is based on the smallest off-the-shelf bearing size obtainable that is placed in the stator (B623B3G, igus®, RI, USA) and the internal jet diameter used. Coupled to the motor is a series of plastic planetary gearboxes, which can be selected to provide a variety of gear-reductions in multiples of 5:1 or 4:1 (72001, Tamiya, Japan). The gear boxes are also 28 mm in diameter (not including the flanges) and each stage is 7.62 mm long. The stator has internal jets (Fig. 2B–C) that redirect the airflow from the inlets to attack the rotor at an angle α (Fig. 2D). The rotor rotates on two bearings (B6800B3G and B623B3G, igus®, RI, USA) that are recessed into the cap and the stator. The cap has six exhaust ports that taper outward to reduce pressure losses associated with sudden expansions [37]. The motor is assembled using plastic hardware (screws, all-thread rod, and hex nuts), all of which are listed in the bill of materials shown in Table I. The rotor and stator are aligned using dowel pins that ensure concentric alignment of the rotor's bearings. The expanded view of the assembly can be seen in Fig. 3.

The Computer Aided Design (CAD) is parametrically designed using equations and global variables to define the motor geometry. This enables quick modification of the design for the specific applications (i.e. torque, rotational speed, and size requirements). The encoder remains the same size for all motor sizes. The global variables are: (1) rotor outer diameter, (2) rotor inner diameter, (3) rotor blade length, (4) nozzle diameter, and (5) nozzle angle of attack. Of these parameters, the rotor inner diameter and the nozzle angle of attack are minimized to maximize torque output and rotational speed, and the rotor blade length is minimized to reduce the overall length of the motor. Thus, the user only needs to change two parameters to modify maximum torque and maximum rotational speed: (1) the rotor outer diameter and (2) the nozzle diameter. These two parameters affect the maximum torque and maximum rotational speed given mass flow rate and density of the air as follows [36]

$$\tau = \frac{\dot{m} \cdot |\dot{m}| \cos(\alpha)}{\rho \cdot A_{nozzle}} (r_1 - r_2) \eta_\tau \tag{1}$$

$$\omega = \frac{\dot{m} \cos(\alpha)}{n r_1 \rho \cdot A_{nozzle}} \eta_\omega \tag{2}$$

where τ is the maximum torque, ω is the maximum rotational speed, $\dot{m}$ is the mass flow rate of the air, ρ is the density of the air, r_1 is the outer radius of the rotor, r is the inner radius of the rotor, n is the number of nozzles per inlet (i.e., 3), A_{nozzle} is the nozzle area, η_τ is the efficiency at the stall torque, and η_ω is the efficiency at the terminal rotational speed of the rotor. It should be noted that it has been observed that $\eta_\tau \approx \eta_\omega \approx 0.55$. Using (1) and (2), and taking into consideration the use of the planetary gearboxes, an appropriately sized motor can be selected to meet a variety of torque and speed applications.

B. Encoder Design

The MR-safe encoder consists of an encoder housing and four fiber optic cables (FDPF 4001 EH, Fibre Data, USA) (Fig. 4A). The encoder housing is 3D-printed using Tough 2000 resin (as opposed to Clear resin) with a FormLabs 3D printer (Form 3B, FormLabs, MA, USA). This opaque resin is used to prevent ambient light from creating a high signal on the receiver channels of the encoder. Of the four fiber optic cables, two are receivers and two are transmitters. Note that the optical fibers are 10-m in length. This is to keep all circuitry in the control room, enabling complete decoupling of the electronics from the MR scanner and preserving MR imaging quality. The receiver channel A is located on the side with the receiver of channel B to prevent cross-talk from their transmitters, as shown in Fig. 4A. The light transmission data is interpreted using an off-the-shelf educational fiber kit that includes a transmitter and receiver circuit (IF E22, Industrial Fiber Optic, USA). The transmitters provide a constant supply of light to the encoder. When the receivers receive this light, the signal is interpreted as high (i.e. 5V); conversely, when the receivers do not receive this light, the signal is interpreted as low (i.e. 0V). To enable quadrature encoding, the fibers are angled toward the rotor shaft. The rotor shaft has a slit in it to act as a light interrupter (Fig. 4A, Section A-A). As the rotor rotates the light from the transmitters is interrupted in a sequential manner that results in standard quadrature encoding, as shown in the oscilloscope screen in Fig. 4B.

III. Fabrication Instructions

A. Motor Fabrication Instructions

The MR-safe motor is fabricated using the FormLabs SLA printer with an orientation as shown in Fig. 5. Note that this orientation is used to ensure that the circular geometry of the rotor, stator, and cap are in the X-Y plane of the printer. The layer height in the slicing operation should be set to 0.050 mm. Following the printing process, the printed components are post processed in the Form Wash for 8 minutes in 90% isopropyl alcohol (IPA). The parts should then be removed from their supports and rinsed for 1 minute in a separate basin of 90% IPA. It is then advised to dry off the motors using compressed air (30 psi-gauge with 1/8” tubing). Additionally, air at 90 psi-gauge should be administered through the inlets of the stator for 10–15 seconds. Note that this should be done over a basin or sink to ensure the residual resin is collected, avoiding ejection onto the floor. All the components can then be cured in the Form Cure for the recommended time and temperature based on the selected resin (Tough 2000 cures at 70°C for 60 minutes). After curing, these parts should not come in contact with IPA, as the resins intentionally degrade when in contact with IPA. However,

some FormLabs resins are compatible with IPA (Surgical Guide Resin, FormLabs, USA), while others can be autoclave steam sterilized.

Following the curing procedure, all the threads should be tapped. These include the following: (1) the three M2x0.4 threads in the stator for motor assembly, (2) the two M2x0.4 threads in the stator for mounting the encoder, (3) the two M5x0.8 threads in the stator for the pneumatic inlets, (4) the three M3x0.5 threads in the flanges of the motor cap, and (5) the three M3x0.5 threads in the gearbox cap for mounting of the entire assembly to a surface. All threads listed above should be tapped all the way through, and the parts should be supported using standard fixturing techniques (i.e. a cushioned vice). The authors prefer to use a drill to rotate the tap at the lowest speed setting to avoid the need for manual tapping. Additionally, small amounts of 90% IPA may be used as a tapping lubricant to ease the tapping process. After tapping the threads, the pneumatic fittings of choice (5463K557, McMaster, USA) should be connected to the stator and air should again be forced through the jets and nozzle. It is advised to use air at 90 psi-gauge and to administer this pneumatic flow for 10–15 seconds.

The rotor requires the attachment of the plastic sun gear provided in the planetary gearbox kit listed in the bill of materials. The rotor is designed to ensure the sun gear has a light press fit. To attach the sun gear, a deep-well socket (such as a 1/2” deep-well socket) should be used to support the rotor from the back in a vice. This socket prevents the thin shaft used for encoding from bearing the load. The sun gear is then placed in front of the recess at the front of the rotor and the vice is used to press the sun gear into the recess. It is strongly advised to include three small drops of cyanoacrylate on the cylindrical surface of the recess. The bearings (B6800B3G and B623B3G) can then be mounted to the rotor.

The motor can now be assembled using the associated plastic hardware listed in the bill of materials (Table I). Using the all-thread (98831A760, McMaster, USA) and the corresponding hex nut (94905A005, McMaster, USA), a stud of appropriate length (based on the number of gearbox stages) can be created that attaches the gearbox to the motor assembly. This stud is used due to the unavailability of offthe-shelf plastic bolts of this length. It is advised to use the provided DC motor in the planetary gearbox kit (72001, Tamiya, Japan) to run the gearbox for 2 minutes or more. This operation hones the gears for smoother operation. The gearbox can now be assembled to the motor, resulting in the finished assembly of the motor and gearbox (excluding the encoder). Note that due to the low cost of the motor, the authors typically apply glue to the flanges that mount the gearbox to the motor. This is to ensure that the studs do not vibrate loose. In the event that a malfunction occurs, a new low cost motor can be made. Note that this should only be done after smooth motor operation is confirmed.

B. Encoder Fabrication Instructions

The MR-safe encoder is fabricated using the FormLabs SLA printer with an orientation as shown in Fig. 5. The washing and curing steps used for post processing the encoder are identical to the post processing steps of the motor. Note that the encoder does not possess any threads; however, before curing, pressurized air should be used to clear out the internal fiber optic guides. After clearing the guides, curing can be performed.

After curing, a strip of fiber optic cable should be used as a tool to clear out the fiber optic cable guides once more in the encoder. This tool can be made by stripping approximately 1” of the fiber optic jacket from a piece of the fiber optic cable and reciprocating the fiber through the encoder guide. Now the encoder operation must be validated. To do this, four fiber optic cables must be cut to an arbitrary length (<0.2-m as these cables will be thrown away). Approximately 1/8” of the fiber optic jacket should be removed from the fiber optic cable at each end using a pair of strippers (IC-375, Jonard Tools, China). Using a specialized high-grit polishing kit (HFBR-4593Z, BROADCOM, USA), both ends of the fiber optic cable should be polished in a planar manner using a figure-eight pattern. Care should be taken to ensure that the polishing creates a cross-section that is perpendicular to the longitudinal axis of the fiber. After the polishing operation, one end of each fiber optic cable should be placed in the corresponding transmitter and receiver position for channel A and channel B. The other end of the fiber optic cable, which will go into the encoder, should have an additional 1/2” of the fiber optic jacket removed (i.e. a total of 5/8”). Using an oscilloscope, the transmitters and receivers should then be placed in the encoder in a configuration similar to Fig. 4A until both signals read as high (i.e. > 4.5V). Then, the encoder should be placed on the motor and the quadrature operation should be validated using the oscilloscope. Following validation, the fiber optic cable inclusion procedure listed above should be performed again using fiber optic cables at the appropriate length (i.e. 10-m for MRI-conditional devices). Once finished, the fiber optic jacket should be epoxied to the encoder housing to restrict motion.

C. Motor Control Setup

In this section, we describe the system setup for the implementation inside the MRI scanner, depicted schematically in Fig. 6. A Simulink xPC target machine is used to control two on/off, normally closed, solenoid valves (2v025–08, Tailonz, USA) using two N-channel power MOSFETs (RFP30N06LE). The valves are connected to a compressed air supply (8010, California Air, USA) that is regulated to 80 psi. The valves are connected to the motor using 10-m pneumatic tubing (5233K52, McMaster, USA). The encoder fiber optic cables are connected to the transmitter/receiver boards, which transmit electrical signals back to the xPC target machine. Using a bang-bang control algorithm that switches the the flow inlet based on the sign of the motor error, an output shaft accuracy of ±20° an be achieved for the smallest motor configuration using a 100:1 gear reduction (rotational speed of 345 rpm). Note that in our experience, this motor configuration is most commonly used while coupled to a lead screw due to the fast rotational speed. Using a 10–32 lead screw (98873A105, McMaster, USA), a 20° error would result in a translation error of 0.04 mm. For rotational operations, we often use a 500:1 gear reduction, which results in a rotational error of ±4° due to encoding at the input shaft. Note that due to the considerable time delay induced by the 10-m pneumatic tubing, which substantially affects the closed-loop stability of the system, a dead-zone region has been incorporated in the control with the bound of 20 degree in output shaft (i.e. control input is zero for position error of ± 20°). This modification enables the system to reach a desired error with minor oscillation.

IV. Results and Discussion

A. Motor Examples and Parameter Selection

To highlight the scalability of the motor, we have printed three different motors (Fig. 1). Each motor had the same blade length (10 mm), rotor inner diameter (11 mm), angle of attack (20°), and nozzle diameter (2 mm). However, each motor used a different rotor outer diameter: 19 mm (our nominal motor design), 35 mm (rotor size from [18]), and 61 mm. A torque and power curve for each motor using a 100:1 gear reduction was generated using an electromagnetic brake (B6–12-2, Placid, USA). The system input pressure was 80 psi-gauge and a 10-m pneumatic transmission line (5233K52, McMaster, USA) was used. The torque and power curves can be seen in Fig. 7. Note that with increasing rotor diameter, the torque increases while the speed decreases. However, the peak power of each curve remains within 10% variation, which is to be expected since the pneumatic input power remains unchanged. Differences in the peak power can be explained by printing tolerances which affect the mass flow rate. The motor model was able to predict the maximum motor torque and speed with a mean error of 15.6% and 14.6%, respectively (see Table II). It should be noted that the largest error occurs with motor using a 61 mm OD rotor, which is likely due to the complexities associated with pneumatic modeling and fluidic uncertainties from manufacturing tolerances.

B. MR-Safe Encoder Validation

The MR-safe optical encoder was validated by coupling the motor to a commercially available encoder (E6C2-CWZ6C 1000P/R 2M, Omron Automation, USA). For validation, the motor was connected to a 100:1 gearbox configuration. Note that the gear transmission possessed a mechanical backlash of $\pm 8^{\circ}$. Each encoder was connected to a Simulink xPC target machine and positional data was recorded at an update rate of 1 kHz. The motor was commanded to spin continuously at a pressure of 80 psi-gauge. The gearbox output shaft rotated 58000° in 14.5 seconds, during which the positional error between the two encoders remained below the mechanical backlash of the system (Fig. 8). The final steady-state error between the two encoders was 0°. This suggests that our MR-safe quadrature encoder is effective at tracking motor position.

C. MR-Safety Validation

MR-safety validation was performed in a 3T Philips MR scanner. The motor was placed close to a CuSO4 phantom bottle. T_1 sequence images were obtained using TE (4.6 ms), TR (10 ms), FA (15°), Resolution ($0.5 \times 0.5 \times 1.3$ mm^3) (see Fig. 9). Image artifact was defined as a change in the pixel intensity of over 30% due to the presence of the motor. SNR was calculated based on [38]. No noticeable image artifact or significant SNR variation (< 1%) was observed during the experiment. MR test according to the F2052 and F2213 standards were also performed [16], [17]. No magnetically induced forces and torques were observed in the experiment and the motor can be safely classified as MR-safe due to the absence of metallic materials and electrical signals.

D. Motor Applications

The proposed motor, and its previous iterations, have been used in a wide variety of applications. In prostate needle placement for focal laser ablation, this motor has been able to place a needle template with an overall targeting accuracy in *ex-vivo* tissue with an accuracy of 2.17±0.47 mm [39] and in canine studies with an accuracy of 0.9±0.47 mm [4]. However, it should be noted that the stages directly controlled by the motor were able to provide sub-millimeter positional accuracy [40], [41]. Due to the accuracy performance achieved by the motor, it has also been used in many other high-risk procedures, such as microinjector intraocular pressure regulation [42] and intracerebral hemorrhage (ICH) evacuation using concentric tubes [3], [5]. In ICH evacuation robot development, the motor was able to provide distal tip placement accuracy of less than 1.75 mm [3], [4]. In more recent work using large diameter plastic tubes (OD: 6 mm), the motor was able to provide distal tip positioning accuracy of less than 1 mm [5]. Another positive feature of this motor is the ability to operate with real-time MR-imaging guidance [5]. For example, this motor has also been used in MR-conditional experimental test-beds embedded with real-time tracking systems [43]. These numerous studies of this motor validate its efficacy and generalizability. Note that the most recent use of this motor found in [5], which uses the current motor design at its smallest feasible dimension (28 mm OD), has been used for over one year without replacement or repair.

E. Broader Dissemination During ISMR

The authors plan to organize a mini-workshop on the fabrication of the motor to expedite the adoption of this motor during the 2023 International Symposium of Medical Robotics (ISMR). During the training, the authors will provide the hands-on fabrication practise for the participants to fabricate their own motor, develop the control mechatronics, and implement the control. The material and supplies will be covered by the authors' lab at Georgia Tech.

V. Conclusion

This paper presents the open source design and manufacturing guidelines of PRIME, a MR-safe pneumatic radial inflow motor and encoder (PRIME). The motor consists of five modifiable global parameters, ensuring scalability, that define the entire geometry of the motor assembly. PRIME is manufactured using a Form 3 SLA printer and consists of off-the-shelf components. Note that in this work the control algorithm and hardware presented focused on the most simple implementation. Future work will investigate a comprehensive, model-based control scheme that accomodate system delay to improve setpoint and trajectory tracking performance.

PRIME has been extensively validated by the authors in a variety of MR-conditional robotics projects, and demonstrated the feasibility and generalizability of the motor hardware. The motor original CAD and quick download STL files will be uploaded to our lab website. We hope this open source motor and encoder design will lower the barrier to entry and eventually benefit a wide range of researchers that are interested in MR-compatible devices and robots.

Acknowledgments

This research is funded by NIH R01 NS116148. The views and opinions of authors expressed herein do not necessarily state or reflect those of NIH.

References

[1]. Elhawary H, Tse ZTH, Hamed A, Rea M, Davies BL, and Lamperth MU, "The case for mr-compatible robotics: a review of the state of the art," The international journal of medical robotics and computer assisted surgery, vol. 4, no. 2, pp. 105–113, 2008. [PubMed: 18481822]

[2]. Chen Y, Poorman ME, Comber DB, Pitt EB, Liu C, Godage IS, Yu H, Grissom WA, Barth EJ, and Webster III RJ, "Treating epilepsy via thermal ablation: initial experiments with an mri-guided concentric tube robot," in Frontiers in Biomedical Devices, vol. 40672, p. V001T02A002, American Society of Mechanical Engineers, 2017.

[3]. Chen Y, Godage IS, Sengupta S, Liu CL, Weaver KD, and Barth EJ, "Mr-conditional steerable needle robot for intracerebral hemorrhage removal," International journal of computer assisted radiology and surgery, vol. 14, no. 1, pp. 105–115, 2019. [PubMed: 30173334]

[4]. Chen Y, Godage IS, Sengupta S, Liu CL, Weaver KD, Barth EJ, and Webster III RJ, "An mri-compatible robot for intracerebral hemorrhage removal," in Frontiers in Biomedical Devices, vol. 40672, p. V001T08A019, American Society of Mechanical Engineers, 2017.

[5]. Gunderman AL, Sengupta S, Siampli E, Sigounas D, Kellner C, Oluigbo C, Sharma K, Godage I, Cleary K, and Chen Y, "A surgical platform for intracerebral hemorrhage robotic evacuation (aspihre): A non-metallic mr-guided concentric tube robot," arXiv preprint arXiv:2206.09848, 2022.

[6]. Franco E, Brujic D, Rea M, Gedroyc WM, and Ristic M, "Needleguiding robot for laser ablation of liver tumors under mri guidance," IEEE/ASME Transactions on Mechatronics, vol. 21, no. 2, pp. 931–944, 2015.

[7]. Stoianovici D, Kim C, Petrisor D, Jun C, Lim S, Ball MW, Ross A, Macura KJ, and Allaf ME, "Mr safe robot, fda clearance, safety and feasibility of prostate biopsy clinical trial," IEEE/ASME Transactions on Mechatronics, vol. 22, no. 1, pp. 115–126, 2016. [PubMed: 28867930]

[8]. Chen Y, Wang W, Schmidt EJ, Kwok K-W, Viswanathan AN, Cormack R, and Tse ZTH, "Design and fabrication of mr-tracked metallic stylet for gynecologic brachytherapy," IEEE/ASME Transactions on Mechatronics, vol. 21, no. 2, pp. 956–962, 2015. [PubMed: 28989272]

[9]. Gunderman AL, Schmidt EJ, Morcos M, Tokuda J, Seethamraju RT, Halperin HR, Viswanathan AN, and Chen Y, "Mr-tracked deflectable stylet for gynecologic brachytherapy," IEEE/ASME Transactions on Mechatronics, vol. 27, no. 1, pp. 407–417, 2021. [PubMed: 35185321]

[10]. Gunderman AL, Schmidt EJ, Viswanathan AN, Halperin HR, Tokuda J, Seethamraju RT, and Chen Y, "Mr-guided tissue puncture with on-line imaging for high-resolution theranostics," in 2020 International Symposium on Medical Robotics (ISMR), pp. 57–61, IEEE, 2020.

[11]. Li G, Patel NA, Hagemeister J, Yan J, Wu D, Sharma K, Cleary K, and Iordachita I, "Body-mounted robotic assistant for mri-guided low back pain injection," International journal of computer assisted radiology and surgery, vol. 15, no. 2, pp. 321–331, 2020. [PubMed: 31625021]

[12]. Patel N, Yan J, Monfaredi R, Sharma K, Cleary K, and Iordachita II, "Preclinical evaluation of an integrated robotic system for magnetic resonance imaging guided shoulder arthrography," Journal of Medical Imaging, vol. 6, no. 2, p. 025006, 2019. [PubMed: 31131290]

[13]. Farooq MU and Ko SY, "A decade of mri compatible robots: Systematic review," IEEE Transactions on Robotics, 2022.

[14]. "Establishing safety and compatibility of passive implants in the magnetic resonance (mr) environment,"

[15]. ASTM F2119, "Test method for evaluation of mr image artifacts from passive implants." www.astm.org, 2013.

[16]. ASTM F2052, "Test method for measurement of magnetically induced displacement force on medical devices in the magnetic resonance environment." www.astm.org, 2015.

[17]. ASTM F2213, “Test method for measurement of magnetically induced torque on medical devices in the magnetic resonance environment.” www.astm.org, 2010.

[18]. Chen Y, Godage IS, Tse ZTH, Webster RJ, and Barth EJ, “Characterization and control of a pneumatic motor for mr-conditional robotic applications,” IEEE/ASME Transactions on Mechatronics, vol. 22, no. 6, pp. 2780–2789, 2017. [PubMed: 31105420]

[19]. Xiao Q, Monfaredi R, Musa M, Cleary K, and Chen Y, “Mr-conditional actuations: a review,” Annals of Biomedical Engineering, vol. 48, no. 12, pp. 2707–2733, 2020. [PubMed: 32856179]

[20]. Krieger A, Song S-E, Cho NB, Iordachita II, Guion P, Fichtinger G, and Whitcomb LL, “Development and evaluation of an actuated mri-compatible robotic system for mri-guided prostate intervention,” IEEE/ASME Transactions on Mechatronics, vol. 18, no. 1, pp. 273–284, 2011. [PubMed: 23326181]

[21]. Li G, Su H, Cole GA, Shang W, Harrington K, Camilo A, Pilitsis JG, and Fischer GS, “Robotic system for mri-guided stereotactic neurosurgery,” IEEE transactions on biomedical engineering, vol. 62, no. 4, pp. 1077–1088, 2014.

[22]. Patel N, Yan J, Li G, Monfaredi R, Priba L, Donald-Simpson H, Joy J, Dennison A, Melzer A, Sharma K, et al. , “Body-mounted robotic system for mri-guided shoulder arthrography: Cadaver and clinical workflow studies,” Frontiers in Robotics and AI, p. 125, 2021.

[23]. Wang Y, Shazeeb M, Sotak C, and Fischer GS, “Optimization of piezoelectric motors to enhance mr compatibility for interventional devices,” in International Society for Magnetic Resonance in Medicine, 17th Scientific Meeting and Exhibition, Proceedings, 2009.

[24]. Comber DB, Slightam JE, Gervasi VR, Neimat JS, and Barth EJ, “Design, additive manufacture, and control of a pneumatic mr-compatible needle driver,” IEEE Transactions on Robotics, vol. 32, no. 1, pp. 138–149, 2016. [PubMed: 31105476]

[25]. Musa MJ, Sharma K, Cleary K, and Chen Y, “Respiratory compensated robot for liver cancer treatment: Design, fabrication, and benchtop characterization,” IEEE/ASME Transactions on Mechatronics, vol. 27, no. 1, pp. 268–279, 2021.

[26]. Pfeil A, Barbe L, Wach B, Bruyas A, Geiskopf F, Nierenberger M, and Renaud P, “A 3d-printed needle driver based on auxetic structure and inchworm kinematics,” in International Design Engineering Technical Conferences and Computers and Information in Engineering Conference, vol. 51807, p. V05AT07A057, American Society of Mechanical Engineers, 2018.

[27]. Stoianovici D, Patriciu A, Petrisor D, Mazilu D, and Kavoussi L, “A new type of motor: pneumatic step motor,” IEEE/ASME Transactions On Mechatronics, vol. 12, no. 1, pp. 98–106, 2007. [PubMed: 21528106]

[28]. Sajima H, Kamiuchi H, Kuwana K, Dohi T, and Masamune K, “Mr-safe pneumatic rotation stepping actuator,” Journal of Robotics and Mechatronics, vol. 24, no. 5, pp. 820–827, 2012.

[29]. Chen Y, Mershon CD, and Tse ZTH, “A 10-mm mr-conditional unidirectional pneumatic stepper motor,” IEEE/ASME Transactions on Mechatronics, vol. 20, no. 2, pp. 782–788, 2014.

[30]. Chen Y, Kwok K-W, and Tse ZTH, “An mr-conditional hightorque pneumatic stepper motor for mri-guided and robot-assisted intervention,” Annals of biomedical engineering, vol. 42, no. 9, pp. 1823–1833, 2014. [PubMed: 24957635]

[31]. Farimani FS and Misra S, “Introducing pneuact: Parametrically-designed mri-compatible pneumatic stepper actuator,” in 2018 IEEE International Conference on Robotics and Automation (ICRA), pp. 200–205, IEEE, 2018.

[32]. Musa M, Sengupta S, and Chen Y, “Design of a 6 dof parallel robot for mri-guided interventions,” in 2021 International Symposium on Medical Robotics (ISMR), pp. 1–7, IEEE, 2021.

[33]. Musa M, Sengupta S, and Chen Y, “Design of a 6 dof parallel robotic platform for mri applications,” Journal of Medical Robotics Research, 2022.

[34]. Comber D and Barth EJ, “Precision position tracking of mr-compatible pneumatic piston-cylinder using sliding mode control,” in Dynamic Systems and Control Conference, vol. 54754, pp. 45–51, 2011.

[35]. Wei Y, Chen Y, Yang Y, and Li Y, “Novel design and 3-d printing of nonassembly controllable pneumatic robots,” IEEE/ASME Transactions on Mechatronics, vol. 21, no. 2, pp. 649–659, 2015.

[36]. Hill PG and Peterson CR, “Mechanics and thermodynamics of propulsion,” Reading, 1992.

[37]. Handbook of Hydraulic Resistance. I. IE, 1986.

[38]. Chinzei K, Kikinis R, and Jolesz FA, “Mr compatibility of mechatronic devices: design criteria,” in International Conference on Medical Image Computing and Computer-Assisted Intervention, pp. 1020–1030, Springer, 1999.

[39]. Seifabadi R, Li M, Xu S, Chen Y, Squires A, Negussie AH, Bakhutashvili I, Choyke P, Turkbey IB, Tse ZTH, et al. , “Mri robot for prostate focal laser ablation: an ex vivo study in human prostate,” Journal of Imaging, vol. 4, no. 12, p. 140, 2018.

[40]. Squires A, Xu S, Seifabadi R, Chen Y, Agarwal H, Bernardo M, Negussie A, Pinto P, Choyke P, Wood B, et al. , “Robot for magnetic resonance imaging guided focal prostate laser ablation,” Journal of Medical Devices, vol. 10, no. 3, 2016.

[41]. Chen Y, Squires A, Seifabadi R, Xu S, Agarwal HK, Bernardo M, Pinto PA, Choyke P, Wood B, and Tse ZTH, “Robotic system for mri-guided focal laser ablation in the prostate,” IEEE/ASME Transactions on Mechatronics, vol. 22, no. 1, pp. 107–114, 2016. [PubMed: 31080341]

[42]. Wineland A, Chen Y, Boland B, Chan K, and Tse Z, “Magnetic resonance conditional microinjector,” Journal of Imaging, vol. 5, no. 1, p. 4, 2018. [PubMed: 34470181]

[43]. Chen Y, Howard J, Godage I, and Sengupta S, “Closed loop control of an mr-conditional robot with wireless tracking coil feedback,” Annals of Biomedical Engineering, vol. 47, no. 11, pp. 2322–2333, 2019. [PubMed: 31218486]

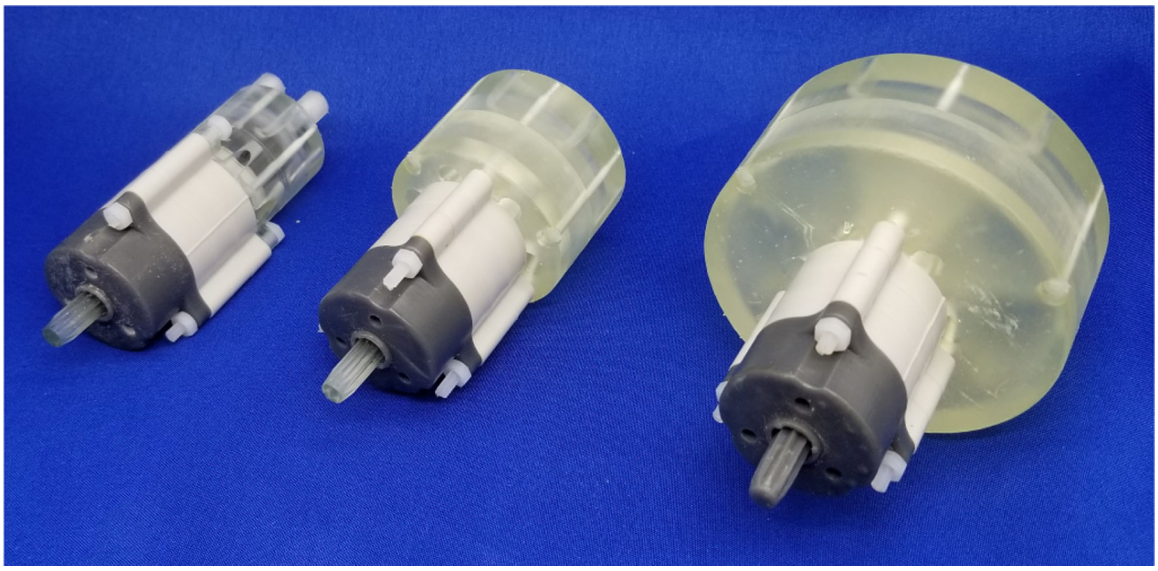

Fig. 1.
Three different scaled motor designs. (Left) Motor with 19 mm OD rotor (authors' nominal preference). (Center) Motor with 44 mm OD rotor (motor size from [18]). (Right) Motor with 61 mm OD rotor.

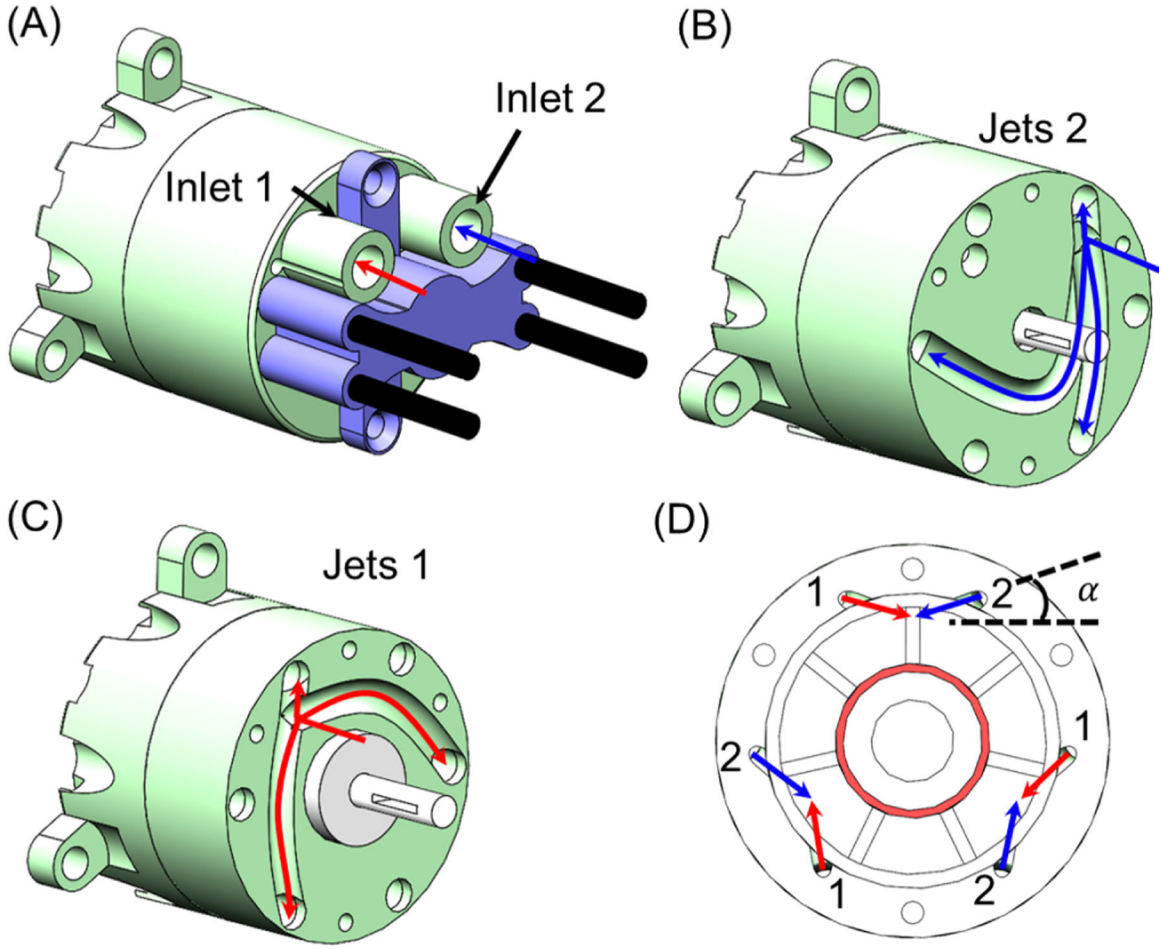

Fig. 2.

(A) The full motor with air stream lines for inlet 1 (blue) and inlet 2 (red) can be seen. (B) The first set of jets that redirect the flow from inlet 1 can be seen in the sectioned motor. (C) The second set of jets that redirect the flow from inlet 2 can be seen in the sectioned motor. (D) The flow can be seen leaving the nozzles with an angle of attack of α.

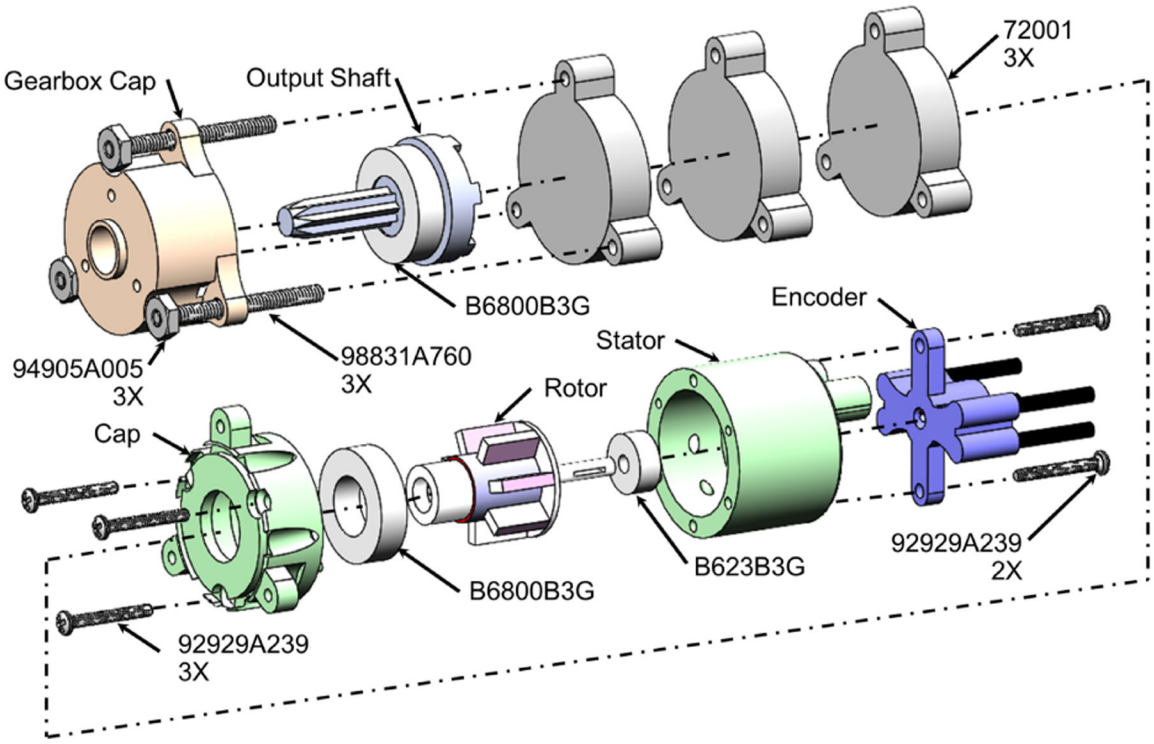

Fig. 3.

The motor assembly in an expanded configuration with trace lines representing the assembly directions. Note that only the general housing shape of the planetary gearbox is modeled.

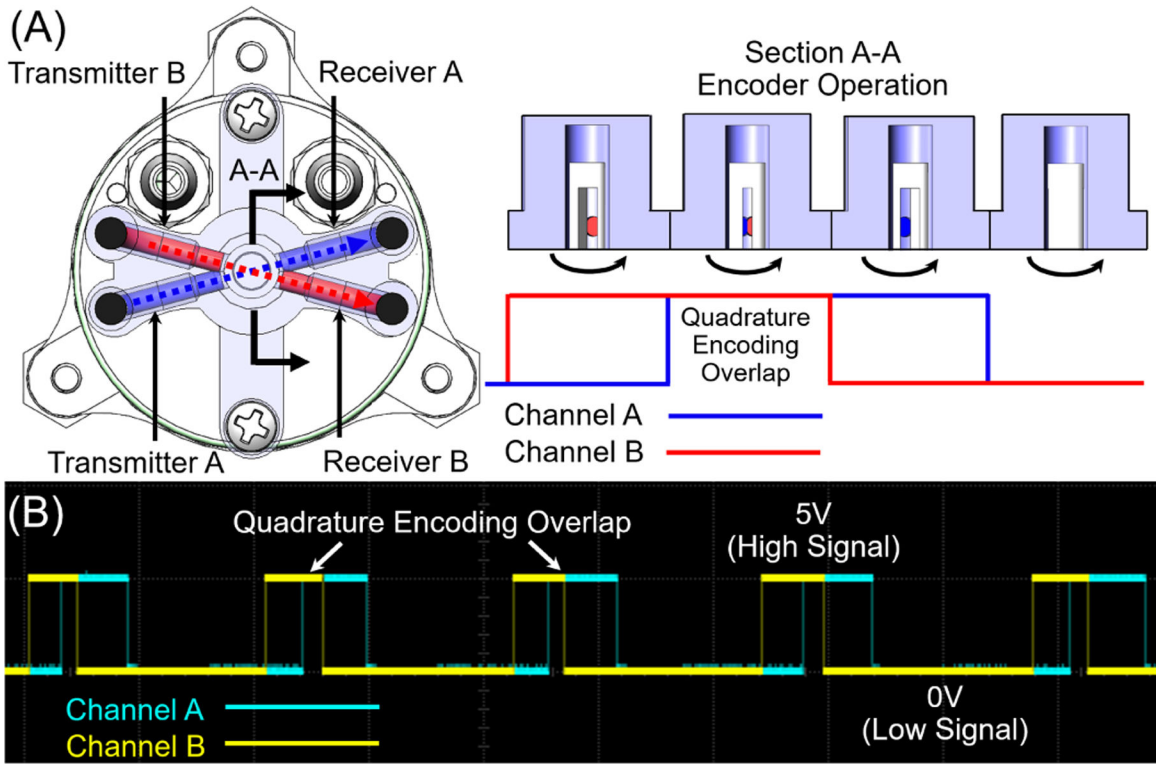

Fig. 4.

(A) Working principle of the quadrature encoder design. Note that receiver A and receiver B are on the same side to avoid cross-talk from the transmitters. (B) The oscilloscope screen capture depicts the electrical signal detected by the proposed encoder.

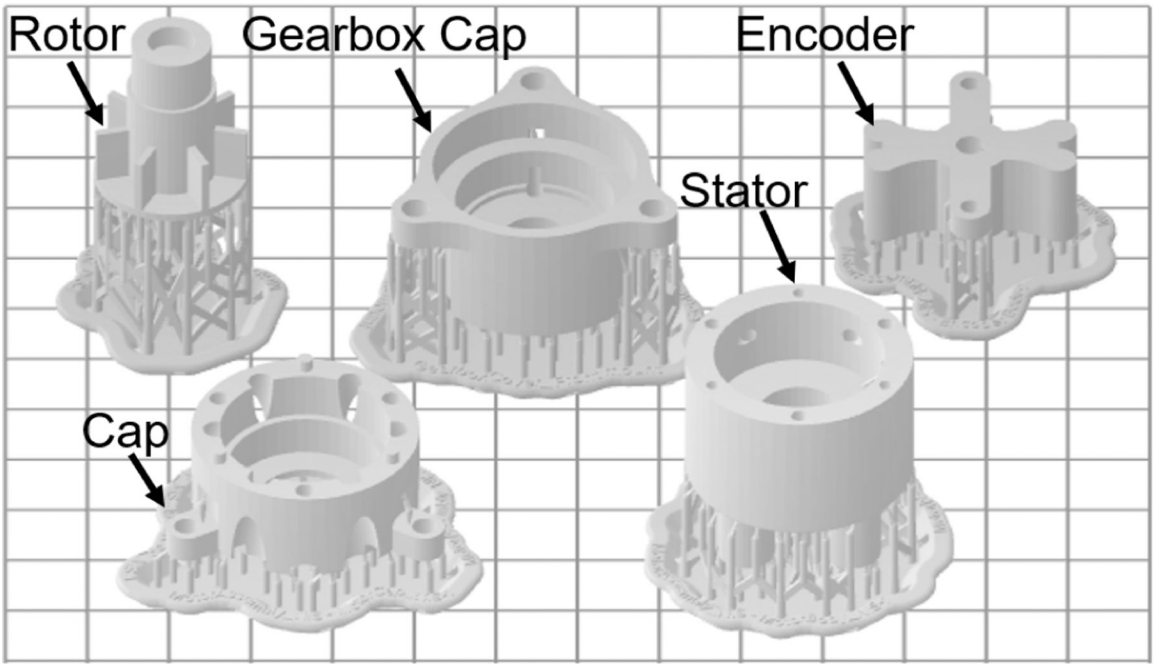

Fig. 5.

The printing setup in the PreForm software can be seen here. Note that this orientation is used to ensure the circular geometry of the rotor, stator, and cap are in the X-Y plane of the printer.

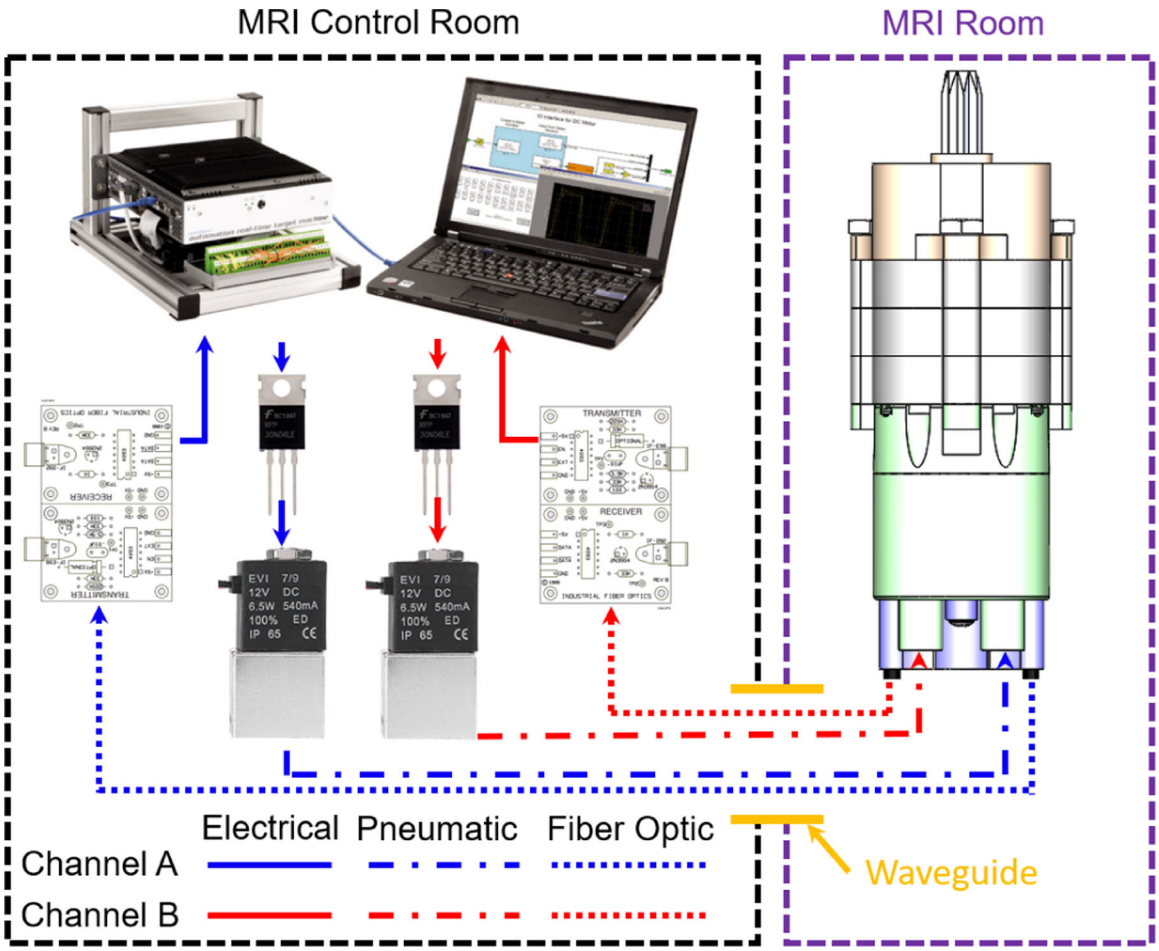

Fig. 6.
Schematic of the system setup for the motor inside the MRI scanner.

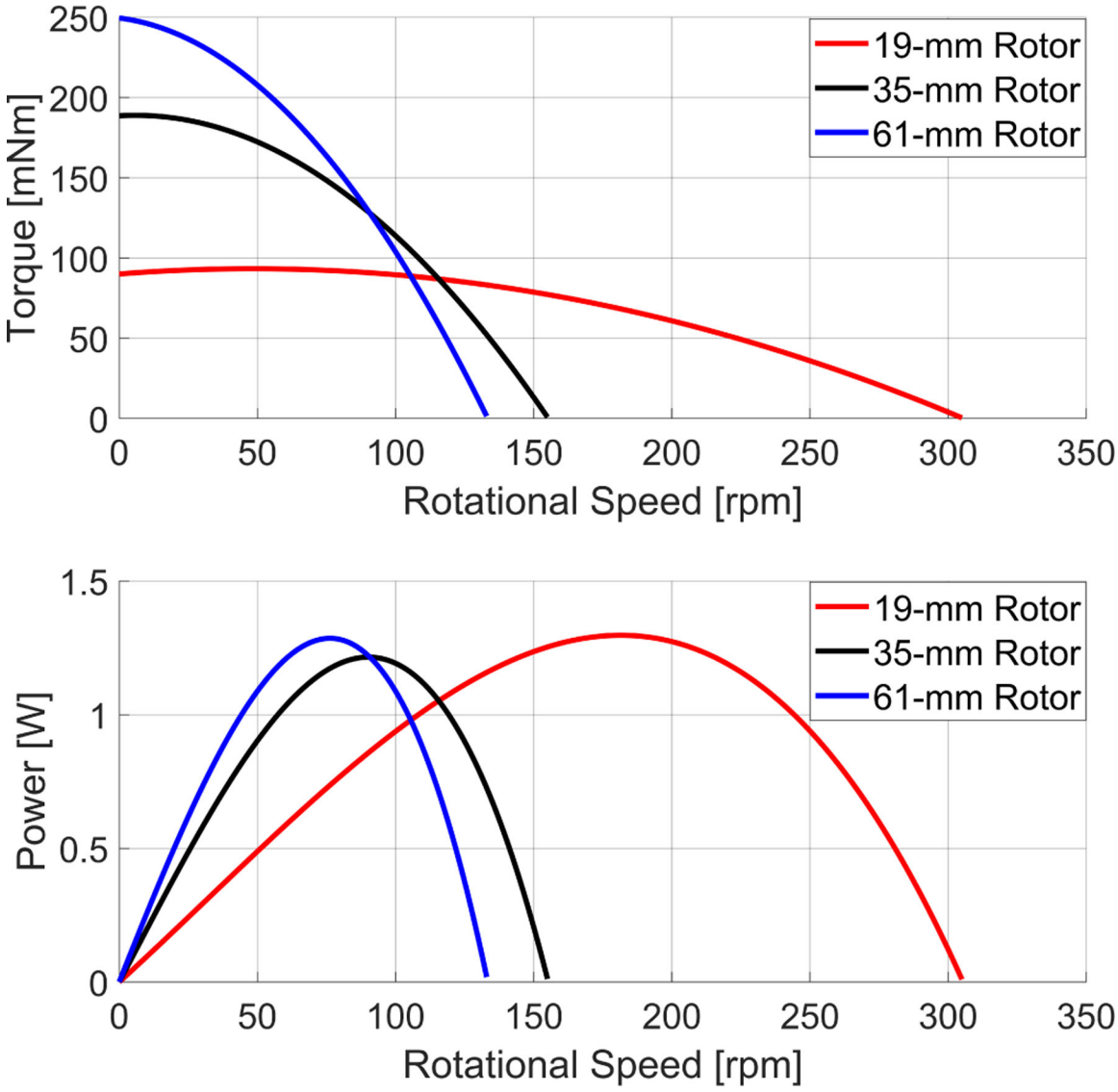

Fig. 7.
The torque (top) and power (bottom) curves of the three different motor designs from Fig. 1.

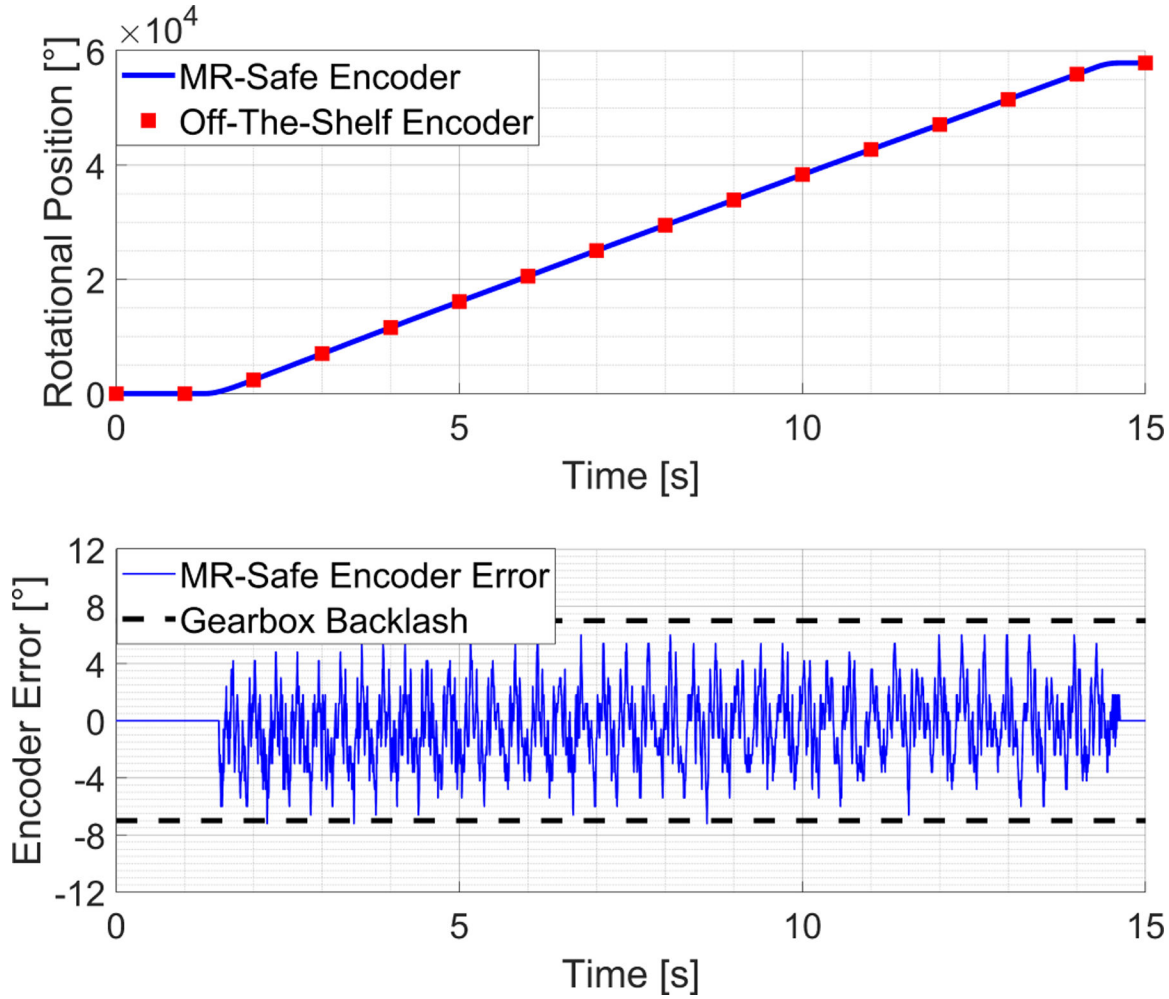

Fig. 8.

(Top) Tracking performance of the encoder (blue) to the commercial encoder (red). (Bottom) Error results of the MR-safe encoder to the off-the-shelf encoder. Note the mechanical backlash of the system was ±8°.

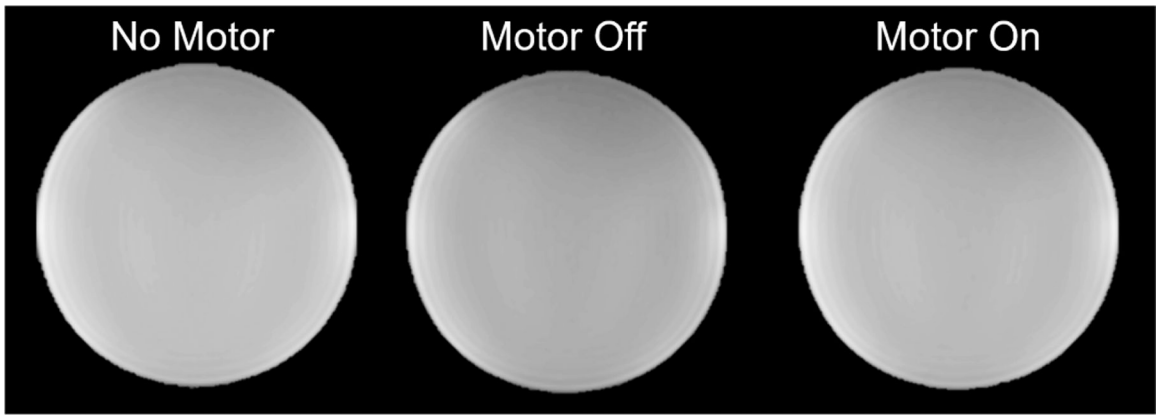

Fig. 9.

T_1-weight images of the phantom can be seen with no motor, with the motor in the scanner and off, and the motor in the scanner and running.

TABLE I

Bill of Materials for Proposed Motor

Item	P/N	Qty.	Vendor	Material	Cost
Stator	N/A	1	FormLabs	Tough 2000 or Clear	$4.03
Cap	N/A	1	FormLabs	Tough 2000 or Clear	$3.13
Rotor	N/A	1	FormLabs	Tough 2000 or Clear	$1.99
Gearbox Cap	N/A	1	FormLabs	Tough 2000 or Clear	$2.98
Output Shaft	N/A	1	FormLabs	Tough 2000 or Clear	$1.84
Planetary Gearbox	72001	1	Tamiya	Plastic	$15.80
Rotor Bearing	B6800B3G	2	igus	Plastic/Glass	$9.48
Rotor Bearing	B623B3G	1	igus	Plastic/Glass	$3.05
Flat Head Screw	92929A239	5	McMaster	Nylon	$0.62
4–40 Threaded Rod	98831A760	3	McMaster	Nylon	$0.58
4–40 Hex Nut	94905A005	3	McMaster	Acetal	$1.05
Encoder Housing	N/A	1	FormLabs	Tough 2000 or Clear	$0.76
Fiber Optic Cable	FDPF 4001 EH	40-m	Fibre Data	Plastic	$27.96
Receiver/Transmitter Kit	IF E22	1	Industrial Fiber Optic	N/A	$18.00
				Total Sum	$91.27

TABLE II

Motor Modeling Results

Rotor OD [mm]	Model Torque [mNm]	Measured Torque [mNm]	Model Speed [rpm]	Measured Speed [rpm]
19	72.2	69.8	295.3	305.0
35	196.4	188.7	152.6	155.0
61	348.6	249.7	80.8	133.0
Mean Error		15.6%		14.6%